

Clifford-deformed Surface Codes

Arpit Dua,^{1,*} Aleksander Kubica,^{2,3,*} Liang Jiang,^{2,4} Steven T. Flammia,^{2,3} and Michael J. Gullans^{5,†}

¹*Department of Physics and Institute for Quantum Information and Matter,
California Institute of Technology, Pasadena, California 91125, USA*

²*AWS Center for Quantum Computing, Pasadena, California 91125, USA*

³*California Institute of Technology, Pasadena, California, 91125, USA*

⁴*Pritzker School of Molecular Engineering, The University of Chicago, Illinois 60637, USA*

⁵*Joint Center for Quantum Information and Computer Science,
NIST/University of Maryland, College Park, Maryland 20742 USA*

Various realizations of Kitaev’s surface code perform surprisingly well for biased Pauli noise. Attracted by these potential gains, we study the performance of Clifford-deformed surface codes (CDSCs) obtained from the surface code by the application of single-qubit Clifford operators. We first analyze CDSCs on the 3×3 square lattice and find that depending on the noise bias, their logical error rates can differ by orders of magnitude. To explain the observed behavior, we introduce the effective distance d' , which reduces to the standard distance for unbiased noise. To study CDSC performance in the thermodynamic limit, we focus on random CDSCs. Using the statistical mechanical mapping for quantum codes, we uncover a phase diagram that describes random CDSCs with 50% threshold at infinite bias. In the high-threshold region, we further demonstrate that typical code realizations at finite bias outperform the thresholds and subthreshold logical error rates of the best known translationally invariant codes.

Optimization of quantum error-correcting (QEC) codes for realistic noise models is one of the essential steps toward fault-tolerant quantum computing. Among QEC codes, Kitaev’s surface code [1–3] and a multitude of its variants [4–8] are perhaps the most experimentally feasible as they can be implemented in two-dimensional architectures with only nearest-neighbor interactions and offer reasonably high circuit noise thresholds. Realistic noise, however, is likely to exhibit bias toward one type of error. For example, in many few-level quantum systems the dephasing rate is much higher than the relaxation rate [9]. Such biased noise is present in the architectures based on superconducting qubits [10], trapped ions [11] and spin qubits [12].

Bias in realistic noise can be beneficial from the perspective of QEC. Two prominent examples are the XY and XZZX surface codes [6, 8]. While both are Clifford-equivalent to the CSS surface code, they both significantly outperform the latter in terms of a threshold against noise biased towards Pauli Z errors [6–8]. Furthermore, for infinite-bias noise, under an appropriate choice of lattice dimensions and boundary conditions, they can also demonstrate an extraordinary subthreshold scaling $\exp[-\mathcal{O}(n)]$ of the logical error rate, where n is the number of physical qubits.

Inspired by these significant improvements, we provide a thorough study of the performance of surface codes against biased noise. For concreteness, we focus on $L \times L$ square lattices, where L is odd, with open boundary conditions; see Fig. 1. We consider stabilizer codes that are obtained from the surface code by the application of single-qubit Clifford operators. We collectively refer to such codes as Clifford-deformed surface codes (CDSCs).

We assume that every qubit is affected by independent and identically distributed (iid) biased Pauli noise with physical error rate $p = p_X + p_Y + p_Z$ and bias η , where

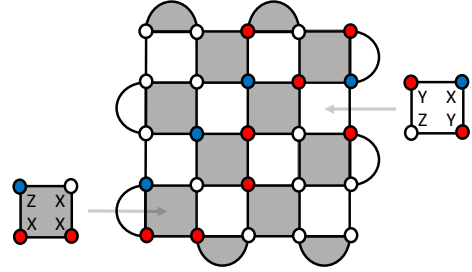


FIG. 1. A Clifford-deformed surface code on the 5×5 square lattice with open boundary conditions. Qubits are on vertices and, in the absence of Clifford deformations, X and Z stabilizer generators are associated with gray and white faces, respectively. To modify the stabilizer group, we apply single-qubit Clifford operations H and $H\sqrt{Z}H$ to blue and red qubits, respectively. We depict two stabilizer generators.

$p_X = p_Y = p_Z/(2\eta)$ are the Pauli error rates. Then, for a given error rate and bias, our goal is to seek CDSCs with optimal performance in terms of either the logical error rate or the code-capacity threshold.

For infinite bias, we explore the threshold phase diagram for random CDSCs and conjecture the existence of a connected region where the corresponding codes have a threshold of 50%. For a moderate noise bias $\eta \sim 100$, we numerically find that typical random CDSCs in the high-threshold region can outperform the thresholds and subthreshold logical error rates of the best known translationally invariant codes, such as the XY and XZZX surface codes.

Clifford deformations.—Given any stabilizer code [13], we can modify its stabilizer group by applying arbitrary single-qubit Clifford operators; we can readily apply Clifford deformations to subsystem codes [14]. Although the resulting code is equivalent (in the sense of a local constant-depth circuit [15, 16]) to the original

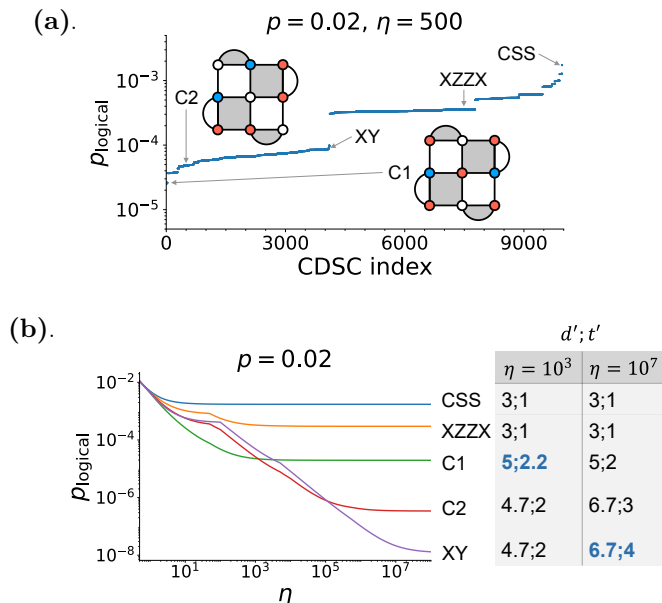


FIG. 2. (a) Comparison of the logical error rate p_{logical} for all possible CDSCs on the 3×3 square lattice against biased Pauli noise with $p = 10^{-2}$ and $\eta = 500$. (b) Logical error rate p_{logical} as a function of the noise bias η for selected CDSCs and fixed $p = 10^{-2}$. Effective distance d' and half-distance t' (up to two leading digits) are shown in the table. For a given η , codes with the highest values $d'; t'$ (colored in blue) perform best.

code, the QEC performance can be improved, especially for biased Pauli noise. This is exemplified by the XZZX surface code [8] that is obtained from the CSS surface code by applying the Hadamard gate H to every other qubit. Note that Clifford deformations can be viewed as a special case of the morphing procedure [17].

We are interested in the QEC performance of the CDSCs against Pauli noise biased towards Pauli Z errors. Since we assume a symmetry between Pauli X and Y errors, *i.e.*, $p_X = p_Y$, it is sufficient to consider Clifford deformations whose action (by conjugation) on the single-qubit Pauli operators is either trivial, or $X \leftrightarrow Z$, or $Y \leftrightarrow Z$. Such Clifford deformations are tensor products of the identity operator I , the Hadamard gate H and $H_{YZ} = H\sqrt{Z}H$.

We construct random realizations of the CDSC by selecting, independently for every qubit, either I , or H , or H_{YZ} with probabilities $1 - \Pi_{XZ} - \Pi_{YZ}$, Π_{XZ} , and Π_{YZ} , respectively. Given Π_{XZ} and Π_{YZ} , we collectively refer to the resulting family of CDSCs as the (Π_{XZ}, Π_{YZ}) random CDSC. Our goal is to understand the performance of a typical realization of the (Π_{XZ}, Π_{YZ}) random CDSC.

The 3×3 layout.—For the representative values of the physical error rate $p = 10^{-2}$ and bias $\eta = 500$ we compare the performance (measured in terms of the logical error rate) of CDSCs on the 3×3 square lattice; Fig. 2(a). Due to the symmetries of the layout and biased Pauli noise, it suffices to consider 9963 codes to catalog all possible performances. Also, for a selection of

codes we study their performance as a function of the noise bias η for fixed error rate $p = 10^{-2}$; Fig. 2(b). For the unbiased noise, *i.e.*, $\eta = 0.5$, all the CDSCs have the same performance, whereas in the regime of the large noise bias, *i.e.*, $\eta \gtrsim 10^6$, the XY surface code provides a clear advantage over other CDSCs, including the CSS and XZZX surface codes. To find the logical error rate we use the maximum-likelihood decoder.

Effective distance.—Although all the CDSCs on the 3×3 square lattice have distance three, their logical error rate can be vastly different. Moreover, codes that perform best change with the noise bias; see Fig. 2(b). To explain this, we introduce the notions of the effective distance d' and half-distance t' of a QEC code for the iid Pauli noise with error rate p and bias η as follows

$$d' = \mathcal{N}^{-1} \log(p_{\text{log}}(1-p)^{-n}), \quad (1)$$

$$t' = \mathcal{N}^{-1} \log(p_{\text{cor}}(1-p)^{-n}), \quad (2)$$

where $\mathcal{N} = \log(p\eta(1+\eta)^{-1}(1-p)^{-1})$ is a normalization factor, n is the number of qubits, p_{log} and p_{cor} are the probabilities of the most likely Pauli operator that, respectively, implements a non-trivial logical operator and is non-correctable. By definition, $t' \geq d'/2$. Also, for the depolarizing noise, which is a special case of the Pauli noise with bias $\eta = 0.5$, we have $p_{\text{log}} = (p/3)^d(1-p)^{n-d}$ and $p_{\text{cor}} = (p/3)^t(1-p)^{n-t}$, where d is the code distance and $t = \lceil (d-1)/2 \rceil$. Thus, $d' = d$ and $t' = t$ for $\eta = 0.5$.

The quantities d' and t' , roughly speaking, capture log probabilities of the most likely non-trivial logical operator and non-correctable error, respectively. Since d' and t' depend on the noise bias η , they constitute a better proxy to the logical error rate than standard code distance d . Note that this proxy is valid whenever p is low and one can ignore entropic factors. Knowing d' and t' allows us to predict which CDSCs on the 3×3 square lattice perform best for the given p and η ; see Fig. 2(b).

Random CDSCs.—To perform a systematic study of CDSC performance in the thermodynamic limit (where a brute-force search of all CDSCs is infeasible for linear size $L > 3$), we now explore the phase space (Π_{XZ}, Π_{YZ}) of all random CDSCs, where, by definition, $\Pi_{XZ}, \Pi_{YZ} \geq 0$ and $\Pi_{XZ} + \Pi_{YZ} \leq 1$; see Fig. 3(a). The $(0, 0)$ and $(0, 1)$ random CDSCs correspond to the CSS and XY surface codes, respectively. Due to the code and noise symmetries, the $(\Pi_{XZ}, 0)$ and $(1 - \Pi_{XZ}, 0)$ random CDSCs are equivalent. We choose the $(0, 0)$ random CDSC to be the reference code to which we apply Clifford deformations. We also note that the XZZX code is a realization of the $(0.5, 0)$ random CDSC.

Infinite bias phase diagram for random CDSCs.—To evaluate the performance of the random CDSCs, we first study their behavior at infinite bias. In particular, we conjecture the existence of a region in the (Π_{XZ}, Π_{YZ}) phase space where the corresponding random CDSCs have a 50% threshold; see Fig. 3(a). We support this conjecture via tensor network simulations for random CDSCs by applying a straightforward adaptation of the tensor network decoder by Bravyi et al. [18],

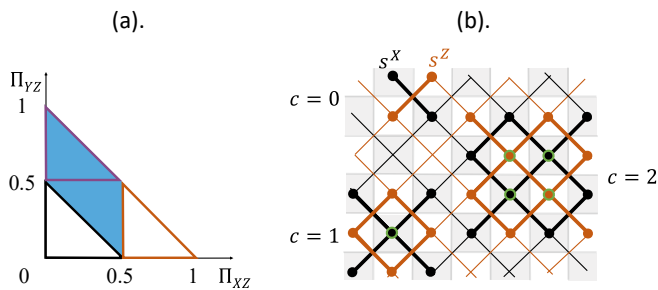


FIG. 3. (a) Phase diagram for the random CDSCs at infinite bias. Typical realizations of random CDSCs in the blue region of the (Π_{XZ}, Π_{YZ}) phase space have a 50% threshold. The black and orange boundaries enclose regions where the s^X and s^Z sublattices order; in the region enclosed by purple boundaries we expect the system to order due to the J_Y constraints. (b) Random-bond Ising model associated with a CDSC; the Hamiltonian is obtained by applying the deformations that define the CDSC to the disordered Hamiltonian in Eq. (3). We also highlight the clusters used in the approximate analytical method to estimate thresholds; see App. B. Spins circled in green are summed over while others are fixed.

which efficiently approximates the maximum likelihood decoder; see App. A and E.

To understand the (Π_{XZ}, Π_{YZ}) phase space, we invoke the connection between the thresholds of QEC codes and the phase transitions in statistical-mechanical classical spin models [3, 19–24]. Using the aforementioned statistical-mechanical mapping, we relate the optimal error-correction thresholds of CDSCs to a critical point along the Nishimori line [25] for a two-dimensional random-bond Ising model (RBIM). For the CSS surface code, which corresponds to the point $(0, 0)$, this RBIM is given by the 8-vertex model [26, 27] whose disordered Hamiltonian (neglecting boundary terms), contains two- and four-body terms, *i.e.*,

$$\mathcal{H}_E = - \sum_{\times} \tau_X J_X \begin{array}{c} \bullet s_i^X \\ \times \\ \bullet s_k^Z \end{array} + \tau_Y J_Y \begin{array}{c} \bullet s_i^X \\ \times \\ \bullet s_k^Z \end{array} + \tau_Z J_Z \begin{array}{c} \bullet s_i^X \\ \times \\ \bullet s_k^Z \end{array}, \quad (3)$$

where $s_*^X, s_*^Z = \pm 1$ are Ising spins associated with every X and Z stabilizer generator of the surface code, and the summation is over the locations of qubits, *i.e.*, all \times and \times crossings; see Fig. 3(b). Moreover, E is a Pauli error for the CSS code that determines the quenched disorder $\tau_P = \pm 1$ via $EP = \tau_P PE$ for every single-qubit Pauli $P = X, Y, Z$ and $J_P = \frac{1}{4\beta} \log \frac{p_E^2(1-p)}{p_X p_Y p_Z}$ is the coupling strength along the Nishimori line with β as the inverse temperature. For the CDSC, depending on the deformation H or H_{YZ} , the relevant Hamiltonian is obtained from Eq. (3) by permuting the corresponding coupling constants $\tau_X J_X \leftrightarrow \tau_Z J_Z$ or $\tau_Y J_Y \leftrightarrow \tau_Z J_Z$, respectively.

Since for $\eta = \infty$ there are only Pauli Z errors, the sign disorder for the coupling constant J_Z in Eq. (3) is fixed, *i.e.*, $\tau_Z = 1$. Moreover, $J_X = J_Y$ and $J_Z = \infty$. Thus, the product of any spins that are coupled by J_Z has to be 1. In other words, depending on the Clifford deformation,

we obtain the following constraints

$$I : \begin{array}{c} \bullet s_i^X \\ \times \\ \bullet s_k^X \end{array} = 1, \quad H : \begin{array}{c} \bullet s_l^Z \\ \times \\ \bullet s_k^Z \end{array} = 1, \quad H_{YZ} : \begin{array}{c} \bullet s_l^X \\ \times \\ \bullet s_k^X \end{array} = 1, \quad (4)$$

which we call J_X , J_Z and J_Y constraints, respectively. Note that the stabilizers that are violated due to the Z error on a qubit correspond to the spins involved in the constraint at that qubit.

We first focus on the point $(0.5, 0)$, which is an extreme point of the 50% threshold region. To understand it, we start from the $(0, 0)$ point and move toward it along the Π_{XZ} axis by applying H deformations. Since H permutes the coupling constants $\tau_X J_X \leftrightarrow \tau_Z J_Z$, we get a correlated bond percolation problem for the J_X and J_Z constraints on the s^Z and s^X sublattices, respectively. For $\Pi_{XZ} < 0.5$, *i.e.*, below the critical point for the bond percolation problem, the J_X constraints do not percolate. However for $\Pi_{XZ} = 0.5$, both the J_Z and J_X constraints exhibit critical fluctuations. Notably, the probability of finding a connected cluster of weight A of J_X and J_Z constraints on the s^Z and s^X sublattices, respectively, scales as $\mathcal{O}(1/A^\tau)$, where $\tau = 187/91$ is the Fisher exponent, while the weight of the largest cluster in the system scales as L^a for $a = 2/(\tau - 1)$ [28]. There is also an important relation between the perimeter of the critical clusters P and their area $A \approx P^{4a/7}$ [29].

We now provide a heuristic argument that these critical clusters of constraints (*i.e.*, infinite strength couplings) are sufficient to order the entire system. Assume that we are in the ordered phase and take a droplet, *i.e.*, a simply connected region of perimeter ℓ and area $A_\ell \geq \ell$. Fixing $3/4 > \epsilon > 0$, the probability Π_ℓ that this droplet has an overlap with at least one critical cluster of perimeter $P \geq \mathcal{O}(\ell^{1+\epsilon})$ scales as $\Pi_\ell \approx A_\ell / \ell^{(1+\epsilon)4a(\tau-2)/7} \geq \mathcal{O}(\ell^{1-(1+\epsilon)5/84})$. Thus, Π_ℓ converges to one with increasing ℓ . Due to the spin constraints, reversing the spins in such a droplet also requires flipping the spins in the entire critical cluster, thereby, leading to a large energetic cost for typical disorder realizations along the Nishimori line, $\beta \Delta \mathcal{H}_E \geq \mathcal{O}(\ell^{1+\epsilon})$, that scales with the cluster perimeter ℓ . Applying Peierls' argument [30], the energetic cost of flipping the spins in such a droplet will typically dominate the entropic contributions to the free energy arising from the number of droplets $N_\ell < 4^\ell$ with perimeter ℓ . As a result, at any finite temperature, droplets with large perimeters will be prevented from fluctuating by the critical clusters of spin constraints. Thus, the ordered phase along the Nishimori line is stable against the proliferation of macroscopic droplets of area $\mathcal{O}(L^2)$ for any finite temperature as $L \rightarrow \infty$. Based on these arguments, we conjecture that RBIMs corresponding to typical realizations of the $(\Pi_{XZ}, \Pi_{YZ}) = (0.5, 0)$ random CDSC remain ordered at any finite temperature along the Nishimori line in the thermodynamic limit, which implies that the $(0.5, 0)$ random CDSC threshold is 50%. Numerical simulations confirm our predictions; see App. E.

We now note that connected clusters of constraints that span the lattice imply the existence of a logical op-

erator made of Pauli Z 's supported on the same qubits as the cluster constraints. In our case, due to the duality of the two sublattices, one of the critical percolation clusters on the two sublattices is spanning and the logical operator is supported on it. In two dimensions, numerical estimates of the typical length of the minimum spanning path indicate the scaling $\mathcal{O}(L^{1.1})$ [28]. This implies that the Z distance (defined as the weight of the minimum-weight logical operator made of Pauli Z 's) for the $(0.5, 0)$ CDSC scales as $\mathcal{O}(L^{1.1})$.

The $(0, 0.5)$ point is another extreme point of the 50% threshold region. Since H_{YZ} permutes the coupling constants $\tau_Y J_Y \leftrightarrow \tau_Z J_Z$, we get a correlated percolation problem of J_Y and J_Z constraints along the Π_{YZ} axis for $\Pi_{XZ} = 0$. Notably, the J_Y constraints involve both s^X and s^Z sublattices. The J_Z constraints on the s^X sublattice percolate for $\Pi_{YZ} \leq 0.5$. However, we expect that only at $\Pi_{YZ} = 0.5$ both J_Z and J_Y constraints percolate. Since the s^X sublattice orders, due to the J_Y constraints, we get effective J_X constraints on the s^Z sublattice. Hence, following similar arguments as above, at $\Pi_{YZ} = 0.5$, the system orders until infinite temperature with an associated 50% threshold.

We now describe the region $\Pi_{YZ} \geq 0.5$. Recall that the $(0, 1)$ random CDSC has 50% threshold [7] and its associated RBIM has J_Y constraints on all qubit locations. Thus, the free energy cost of insertion of a disorder domain wall corresponding to a logical made of Pauli Z 's in the RBIM diverges with L for any finite temperature. This suggests that a macroscopic connected cluster of J_Y constraints can be sufficient to order the system in a phase space region defined by $\Pi_{YZ} \geq 0.5$. Hence, the random CDSCs have a 50% threshold.

Lastly, for the region $\Pi_{XZ} + \Pi_{YZ} > 0.5$ and $\Pi_{XZ}, \Pi_{YZ} < 0.5$, the J_Y constraints combine with the J_X/J_Z constraints to form a macroscopic cluster of constraints on the s^Z/s^X sublattices, respectively. Similar to the cases considered above, these clusters of constraints will stabilize the ordered phase at any finite temperature in the thermodynamic limit. In fact, the presence of an extensive cluster made jointly out of the J_Y constraints combined with J_X/J_Z constraints on the s^Z/s^X sublattices, suffices to explain the interior of the full phase diagram. At the extreme point $(0, 1)$, such a cluster consists of only J_Y constraints, while it is composed of only J_X or J_Z constraints at the $(0.5, 0)$ point (see above).

Finite-bias performance of random CDSCs.—Moving away from infinite bias, we want to find the (Π_{XZ}, Π_{YZ}) random CDSCs that perform best for a given error rate p and bias η . As a proxy to the logical error rate we could use the effective distance d' and half-distance t' . For instance, for the XY surface code $d'(L) = L - \mathcal{N}^{-1} \log(2\eta)$ in the regime of low p and moderate η . Unfortunately, we do not know efficient methods of calculating d' and t' for any random CDSC, and thus do not analyze these quantities directly. Instead, we introduce a heuristic quantity of the effective distance increment $\Delta d'(L) = d'(L+2) - d'(L)$, where L is the linear

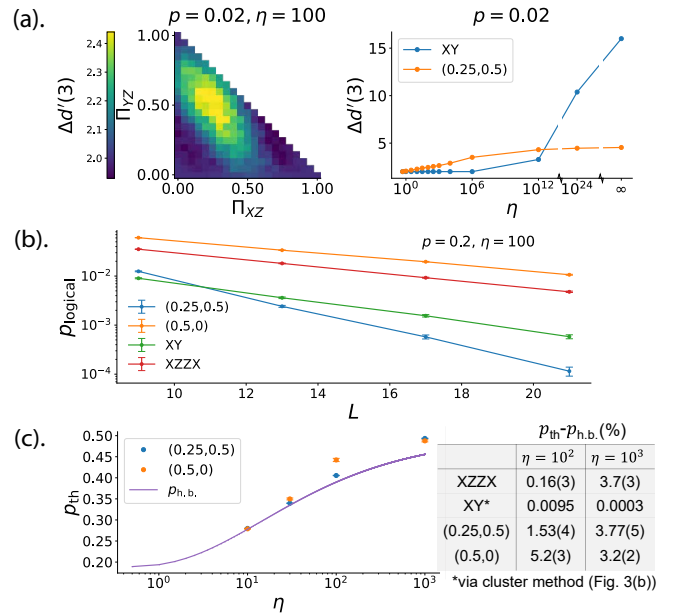


FIG. 4. (a) Effective distance increment $\Delta d'(L = 3)$ for random CDSCs and $p = 0.02$, where we averaged over 2000 realizations for each point. (left) For $\eta = 100$, the highest value is obtained for the $(0.25, 0.5)$ random CDSC. (right) $\Delta d'(3)$ as a function of η . For large η , $\Delta d'(3)$ for the XY surface code starts to increase with η (which is consistent with the Z distance of the XY surface code being L^2 for infinite bias [7]) and exceeds $\Delta d'(3)$ for the $(0.25, 0.5)$ random CDSC. (b) Subthreshold logical error rates p_{logical} of random CDSCs on the $L \times L$ square lattice for $p = 0.2$ and $\eta = 100$. (c) Thresholds p_{th} for the $(0.25, 0.5)$ and $(0.5, 0)$ random CDSCs and the hashing bound $p_{\text{h.b.}}$ as functions of η . The difference $p_{\text{th}} - p_{\text{h.b.}}$ is tabulated in percentage for some codes and biases.

lattice size. We expect $\Delta d'(L)$ to be indicative of random CDSCs with good sub-threshold scaling; see Fig. 4(a).

Now comparing to tensor network simulations, we find that the $(0.25, 0.5)$ random CDSC, which is the best performing code family according to $\Delta d'(3)$, also has the best subthreshold scaling of the logical error rate and outperforms the XY and XZZX surface codes, which we treat as a benchmark; see Fig. 4(b) and App. C. Moreover, its threshold exceeds the hashing bound and the thresholds of the XZZX and XY codes at a moderate bias of $\eta = 100$; see Fig. 4(c).

We remark that the statistical-mechanical mapping for the XY surface code without disorder is self-dual whenever $p_X = p_Y$. Hence, one can use the cluster methods [31, 32] with the clusters in Fig. 3(b) to estimate thresholds at any noise bias η . We describe the method in App. B and show the results for two biases in Fig. 4(c). Extending these methods to the non-self-dual regimes at finite bias (which would apply to other CDSCs) remains an outstanding challenge.

Discussion.—In our work, we introduce the concept of Clifford deformations of QEC codes and use it to construct CDSCs. We observe that for Pauli noise with finite bias η , random CDSCs over a broad range of param-

ters outperform carefully constructed translationally invariant codes, such as the XY and XZZX surface codes. Thus, the choice of Clifford deformation is an important optimization parameter in QEC that goes beyond the choice of the lattice and its boundaries. We expect that exploring spatially non-uniform Clifford deformations or translation invariant ones with bigger unit cells will lead to high-performing QEC codes under biased noise.

In order to leverage the benefits of CDSCs into practical universal computation, we have to implement syndrome measurement circuits and fault-tolerant logical gates in a bias-preserving way. Using equivalence relations under global permutations, our results establish that (similar to the XZZX surface code) the $(0.5, \Pi_{YZ})$ random CDSCs have a 50% threshold for noise infinitely biased towards either Pauli- X , Y , or Z errors. We further expect random CDSCs to have favorable performance when the bias magnitude or direction is non-uniform in

space. Thus, CDSCs may provide an attractive approach to building scalable quantum computers.

Acknowledgements.—We thank David Huse and Giacomo Torlai for valuable discussions and Ali Lavasani for useful feedback on the manuscript. AD thanks Eric Huang for sharing his plotting routines. The tensor network decoder for the random CDSCs was implemented via an appropriate adaptation of *qecsim* [33] (a Python3 package for simulating quantum error correction using stabilizer codes) and simulations were run on the NIST Raritan cluster. The simulation code and data are available on request. This work was supported by the National Science Foundation (QLCI grant OMA-2120757), ARO (W911NF-18-1-0212), the Packard Foundation (2020-71479), the Simons Foundation through the collaboration on Ultra-Quantum Matter (651438, AD) and by the Institute for Quantum Information and Matter, an NSF Physics Frontiers Center (PHY-1733907).

* These authors contributed equally.

† Correspondence: adua@caltech.edu, mgullans@umd.edu

- [1] A. Kitaev, *Annals of Physics* **303**, 2 (2003).
- [2] S. B. Bravyi and A. Y. Kitaev, [arXiv:quant-ph/9811052](https://arxiv.org/abs/quant-ph/9811052) (1998).
- [3] E. Dennis, A. Kitaev, A. Landahl, and J. Preskill, *Journal of Mathematical Physics* **43**, 4452–4505 (2002).
- [4] H. Bombin, *Physical Review Letters* **105**, 030403 (2010).
- [5] T. J. Yoder and I. H. Kim, *Quantum* **1**, 2 (2017).
- [6] D. K. Tuckett, S. D. Bartlett, and S. T. Flammia, *Physical Review Letters* **120**, 050505 (2018).
- [7] D. K. Tuckett, A. S. Darmawan, C. T. Chubb, S. Bravyi, S. D. Bartlett, and S. T. Flammia, *Physical Review X* **9**, 041031 (2019).
- [8] J. P. Bonilla Ataides, D. K. Tuckett, S. D. Bartlett, S. T. Flammia, and B. J. Brown, *Nature Communications* **12**, 2172 (2021).
- [9] A. A. Clerk, M. H. Devoret, S. M. Girvin, F. Marquardt, and R. J. Schoelkopf, *Reviews of Modern Physics* **82**, 1155 (2010).
- [10] P. Aliferis, F. Brito, D. P. DiVincenzo, J. Preskill, M. Steffen, and B. M. Terhal, *New Journal of Physics* **11**, 013061 (2009).
- [11] D. Nigg, M. Müller, E. A. Martinez, P. Schindler, M. Hennrich, T. Monz, M. A. Martin-Delgado, and R. Blatt, *Science* **345**, 302–305 (2014).
- [12] G. Burkard, T. D. Ladd, J. M. Nichol, A. Pan, and J. R. Petta, Semiconductor spin qubits (2021), [arXiv:2112.08863](https://arxiv.org/abs/2112.08863) [cond-mat.mes-hall].
- [13] D. Gottesman, PhD thesis (1997), [quant-ph/9705052](https://arxiv.org/abs/quant-ph/9705052).
- [14] D. Poulin, *Physical Review Letters* **95**, 230504 (2005).
- [15] M. B. Hastings and X.-G. Wen, *Physical Review B* **72**, 045141 (2005).
- [16] X. Chen, Z.-C. Gu, and X.-G. Wen, *Physical Review B* **82**, 155138 (2010).
- [17] M. Vasmer and A. Kubica, Morphing quantum codes (2021), [arXiv:2112.01446](https://arxiv.org/abs/2112.01446) [quant-ph].
- [18] S. Bravyi, M. Suchara, and A. Vargo, *Physical Review A* **90**, 032326 (2014).
- [19] C. Wang, J. Harrington, and J. Preskill, *Annals of Physics* **303**, 31–58 (2003).
- [20] H. G. Katzgraber, H. Bombin, and M. A. Martin-Delgado, *Physical Review Letters* **103**, 090501 (2009).
- [21] H. Bombin, R. S. Andrist, M. Ohzeki, H. G. Katzgraber, and M. A. Martin-Delgado, *Physical Review X* **2**, 021004 (2012).
- [22] A. A. Kovalev and L. P. Pryadko, Spin glass reflection of the decoding transition for quantum error correcting codes (2014), [arXiv:1311.7688](https://arxiv.org/abs/1311.7688) [quant-ph].
- [23] A. Kubica, M. E. Beverland, F. Brandão, J. Preskill, and K. M. Svore, *Physical Review Letters* **120**, 180501 (2018).
- [24] C. T. Chubb and S. T. Flammia, *Annales de l'Institut Henri Poincaré D* **8**, 269–321 (2021).
- [25] H. Nishimori, *Progress of Theoretical Physics* **66**, 1169 (1981).
- [26] C. Fan and F. Y. Wu, *Physical Review B* **2**, 723 (1970).
- [27] B. Sutherland, *Journal of Mathematical Physics* **11**, 3183 (1970).
- [28] D. Stauffer and A. Aharony, *Introduction to percolation theory* (Taylor & Francis London, 1992).
- [29] H. Saleur and B. Duplantier, *Physical Review Letters* **58**, 2325 (1987).
- [30] R. B. Griffiths, *Physical Review* **136**, A437 (1964).
- [31] M. Ohzeki, H. Nishimori, and A. N. Berker, *Physical Review E* **77**, 061116 (2008).
- [32] M. Ohzeki, *Physical Review E* **79**, 021129 (2009).
- [33] D. K. Tuckett, *Tailoring surface codes: Improvements in quantum error correction with biased noise*, Ph.D. thesis, University of Sydney (2020), (qecsim: <https://github.com/qecsim/qecsim>).

Appendix A: Adaptation of the BSV decoder and simulations

The Bravyi-Suchara-Vargo (BSV) decoder [18] is an efficient approximation of the optimal maximum likelihood (ML) decoder [3]. The ML decoder achieves the error threshold same as that obtained from the critical point of the statistical-mechanical mapping of error correction. The BSV decoder achieves a value close to it. Given a particular syndrome configuration, the goal is to calculate the probabilities of logical error classes and provide a correction operator based on the maximal probability logical class. Exact evaluation of the logical error class probabilities is, in general, inefficient. The BSV decoder uses an algorithm that efficiently approximates the logical error class probabilities through tensor-network contractions. The size of the tensors being contracted is reduced through Schmidt decomposition and retaining only the χ largest Schmidt values, *i.e.*, χ is the bond dimension of the tensors. For a modest value of χ , the method converges for a range of noise models and boundary conditions of the surface code.

Our numerical implementation uses a few minor modifications to the BSV decoder for the standard form of the surface code with a uniform noise model. To make these modifications, we keep the Heisenberg picture in mind, *i.e.*, we keep the standard form of the stabilizers but have a spatially varying noise model depending on the Clifford deformations that are applied to the qubits. In the Heisenberg picture, the tensor redefinitions can be understood as having a different local noise model on each qubit leading to the redefinition of the associated tensor. For the random code with a given ratio of Clifford deformations Π_{XZ} and Π_{YZ} , we modify the noise model on each tensor associated with a qubit according to the Pauli permutation acting on it. For example, a local noise model given by (p_X, p_Y, p_Z) maps to (p_Z, p_Y, p_X) under the Hadamard deformation H acting on the qubit. Besides this, errors on the qubits are generated according to the local noise model instead of a uniform noise model due to the extra permutation actions on noise in the Heisenberg picture. We illustrate this for a particular code realization in Fig. 5.

Appendix B: Cluster summation method for Maximum Likelihood thresholds

In this appendix, we describe the approximate analytical method for calculating the critical points of random-bond Ising models (RBIMs) that are self-dual in the absence of disorder [31, 32]. The partition function of the RBIM is given by

$$Z = \sum_{\{s_i\}} \prod_{\{i\}} \text{LBF}(\{s_i\}, \{\tau_P J_P\}) \quad (\text{B1})$$

where $\text{LBF}(\{s_i\}, \{\tau_P J_P\})$ is the local Boltzmann factor (LBF) involving spins $\{s_i\}$ at positions $\{i\}$ in a local

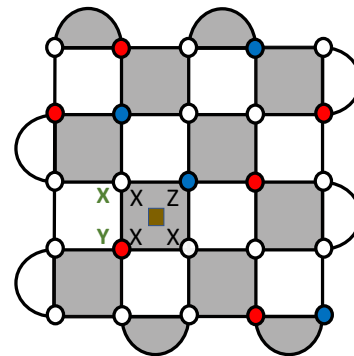


FIG. 5. Example to describe the modification in the evaluation of logical error class probability due to Clifford deformations. Pauli error is shown in green letters. The goal is to evaluate the probability of this error times the stabilizer marked by brown square that appears as a term in the logical error class probability evaluated via tensor network contraction. Without the Clifford deformations, error times the marked stabilizer gives two X operators and one Z operator resulting in a probability $p_X^2 p_Z (1-p)^{L^2-3}$ where p is the total error rate and L^2 is the number of qubits. Because of Hadamard H (blue) and $H_{YZ} = H\sqrt{Z}H$ (red) Clifford deformations acting on two qubits of the marked stabilizer, we instead get three X operators resulting in probability $p_X p_Z^2 (1-p)^{L^2-3}$. Equivalently, we can modify the local noise model on the qubits, according to the Clifford deformations while keeping the stabilizers same as CSS toric code to get the same logical error class probability as with deformed stabilizers and spatially uniform Z bias model.

neighborhood, interacting with coupling coefficients J_P that have sign disorder τ_P . The statistical mechanical model in Eq. (3) is the so-called 8-vertex model. The Hamiltonian (neglecting boundary terms) can be written more explicitly as

$$\mathcal{H} = - \sum_{\times} \tau_X J_X \begin{array}{c} \bullet s_i^z \\ \diagdown \quad \diagup \\ \times \\ \diagup \quad \diagdown \\ \bullet s_k^z \end{array} + \tau_Y J_Y \begin{array}{c} \bullet s_j^x \quad \bullet s_l^z \\ \diagdown \quad \diagup \\ \times \\ \diagup \quad \diagdown \\ \bullet s_k^z \quad \bullet s_i^x \end{array} + \tau_Z J_Z \begin{array}{c} \bullet s_i^x \\ \diagdown \quad \diagup \\ \times \\ \diagup \quad \diagdown \\ \bullet s_l^x \end{array} \\ - \sum_{\times} \tau_X J_X \begin{array}{c} \bullet s_j^z \\ \diagdown \quad \diagup \\ \times \\ \diagup \quad \diagdown \\ \bullet s_l^z \end{array} + \tau_Y J_Y \begin{array}{c} \bullet s_j^z \quad \bullet s_l^x \\ \diagdown \quad \diagup \\ \times \\ \diagup \quad \diagdown \\ \bullet s_k^x \quad \bullet s_i^z \end{array} + \tau_Z J_Z \begin{array}{c} \bullet s_l^x \\ \diagdown \quad \diagup \\ \times \\ \diagup \quad \diagdown \\ \bullet s_k^x \end{array}, \quad (\text{B2})$$

where s_*^X and s_*^Z are Ising spins associated with every X and Z stabilizer generator of the surface code, and the summation is over all qubit locations, *i.e.*, \times and \times crossings; see Fig. 3(b) in the main text.

For the 8-vertex model, the LBF $\{\{s_i\}, \{\tau_P J_P\}\}$ at inverse temperature β for the spins $\{s_i\}$ on a \times is given by

$$\text{LBF}(\{s_i\}, \{\tau_P J_P\}) = \exp \left(\tau_X J_X \begin{array}{c} \bullet s_i^z \\ \diagdown \quad \diagup \\ \times \\ \diagup \quad \diagdown \\ \bullet s_k^z \end{array} + \tau_Y J_Y \begin{array}{c} \bullet s_j^x \quad \bullet s_l^z \\ \diagdown \quad \diagup \\ \times \\ \diagup \quad \diagdown \\ \bullet s_k^z \quad \bullet s_i^x \end{array} + \tau_Z J_Z \begin{array}{c} \bullet s_i^x \\ \diagdown \quad \diagup \\ \times \\ \diagup \quad \diagdown \\ \bullet s_l^x \end{array} \right). \quad (\text{B3})$$

The LBF associated with neighboring qubit of the underlying surface code is similar but with the colors switched,

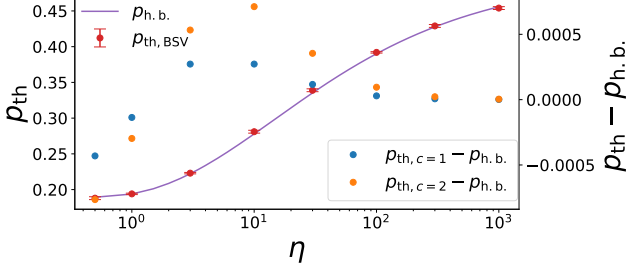


FIG. 6. Cluster-based approximation to the finite-bias threshold. $c = 0$ approximation is same as the hashing bound, *i.e.*, $p_{\text{th},c=0} = p_{\text{h.b.}}$. The difference $p_{\text{th}} - p_{\text{h.b.}}$ of the threshold values (obtained using the BSV decoder [7] and using the different cluster approximations $c = 1, 2$) from the hashing bound is shown.

i.e., \times . To average over the sign disorders τ_P in coupling coefficients J_P , we consider a replicated system with n replicas, whose partition function we can write as follows,

$$Z_n = \langle \left[\sum_{\{s_i\}} \prod_{\{i\}} \text{LBF}(\{s_i\}, \{\tau_P J_P\}) \right]^n \rangle. \quad (\text{B4})$$

Here, $\langle \dots \rangle$ denotes an average over configurations with different disorder realizations. The LBF of the replicated system can be written as follows,

$$\text{LBF}^{(n)}(\{s_i\}, \{J_P\}) = \langle \left[\prod_{\{i\}} \text{LBF}(\{s_i\}, \{\tau_P J_P\}) \right]^n \rangle. \quad (\text{B5})$$

We now consider an n -binary Fourier transform Z^* of the partition function of the replicated system as follows,

$$Z_n^* = \sum_{\{s_i\}} \prod_{\{i\}} \text{DBF}^{(n)}(\{s_i\}, \{J_P\}) \quad (\text{B6})$$

where s_i indicates the spins in a dual lattice and $\text{DBF}^{(n)}(\{s_i\}, n, \{J_P\})$ refers to the dual Boltzmann factor which is given by the n -binary Fourier transformation of the LBF. When the coupling constants J_P are such that the model without quenched disorder is self-dual, then we can equate the partition function and its n -binary Fourier transformation to get a good approximation to the critical point of the disordered statistical mechanical model. This critical point is an approximation of the ML threshold of the error correcting code. The product in the definition of Z_n and Z_n^* is hard to evaluate over the full lattice and can be approximated by taking it over a cluster of spins. The required cluster size increases for a better approximation to the threshold. We show the clusters we used to get the thresholds in Fig. 3(b) of the main text.

We consider the limit $n \rightarrow 1$ to get a good approximation to the critical point of the disordered statistical mechanical model. In this limit, $Z_n = Z_n^*$ reduces to the

following equation,

$$\langle \log \sum_{\{s_f\}} \prod_{\text{cluster}} \text{LBF} \rangle = \langle \log \sum_{\{s_f\}} \prod_{\text{cluster}} \text{DBF} \rangle, \quad (\text{B7})$$

where $\langle \dots \rangle$ denotes the disorder average. The 8-vertex model is self-dual when the coupling coefficients $J_X = J_Z$. The LBF expressed in Eq. (B3) can be written as

$$\text{LBF} = \exp \left[\tau_X J_X s_1^Z s_2^Z + \tau_Z J_Z s_1^X s_2^X + \tau_X \tau_Z J_Y s_1^X s_2^X s_1^Z s_2^Z \right],$$

where s^X denote spins corresponding to the X stabilizers (at the ends of the black bond in Eq. (B3)) and s^Z denote spins corresponding to the Z stabilizers (at the ends of the orange bond in Eq. (B3)). Taking the Fourier transform, we get the dual Boltzmann factor DBF as follows,

$$\begin{aligned} \text{DBF} &= \frac{1}{2} \exp \left[\tau_X J_X + \tau_Z J_Z + \tau_X \tau_Z J_Y \right] \\ &+ \exp \left[\tau_X J_X - \tau_Z J_Z - \tau_X \tau_Z J_Y \right] s_1^X s_2^X \\ &+ \exp \left[-\tau_X J_X + \tau_Z J_Z - \tau_X \tau_Z J_Y \right] s_1^Z s_2^Z \\ &+ \exp \left[-\tau_X J_X - \tau_Z J_Z + \tau_X \tau_Z J_Y \right] s_1^X s_2^X s_1^Z s_2^Z. \end{aligned}$$

$c = 0$ result is same as the hashing bound $p_{\text{h.b.}}$ curve in Fig. 6. We obtained the thresholds $p_{\text{th},c=1}$ and $p_{\text{th},c=2}$ for the XY code using the larger clusters $c = 1$ and $c = 2$ at different values of Z biases η . The difference of the thresholds p_{th} from the hashing bound $p_{\text{h.b.}}$ is also shown in Fig. 6.

Appendix C: Subthreshold scaling plots

In Fig. 7 below, we show the plots depicting subthreshold performance of the random CDSCs, the XY code and the XZZX code at different biases $\eta = 10, 100, 1000$ and physical error rate $p = 0.2$. We calculated the logical error rate from 200 000 Monte Carlo runs for code distances $L = 9, 13, 17, 21$. Each Monte Carlo run for simulating error correction on the random CDSC is done on a different realization consistent with the probabilities (Π_{XZ}, Π_{YZ}) . Error bars were calculated through jackknife resampling. We also include the XZZX on a torus with coprime dimensions $L \times (L + 1)$ using minimum-weight perfect matching (MWPM) decoder for comparison since it has been shown to have extraordinary subthreshold performance as well. However, since the decoder, the number of qubits $(L(L + 1))$ as opposed to L^2 for the square lattice codes) and the boundary conditions are all different, the comparison's goal is only to justify that the random CDSCs can beat the best known subthreshold performance.

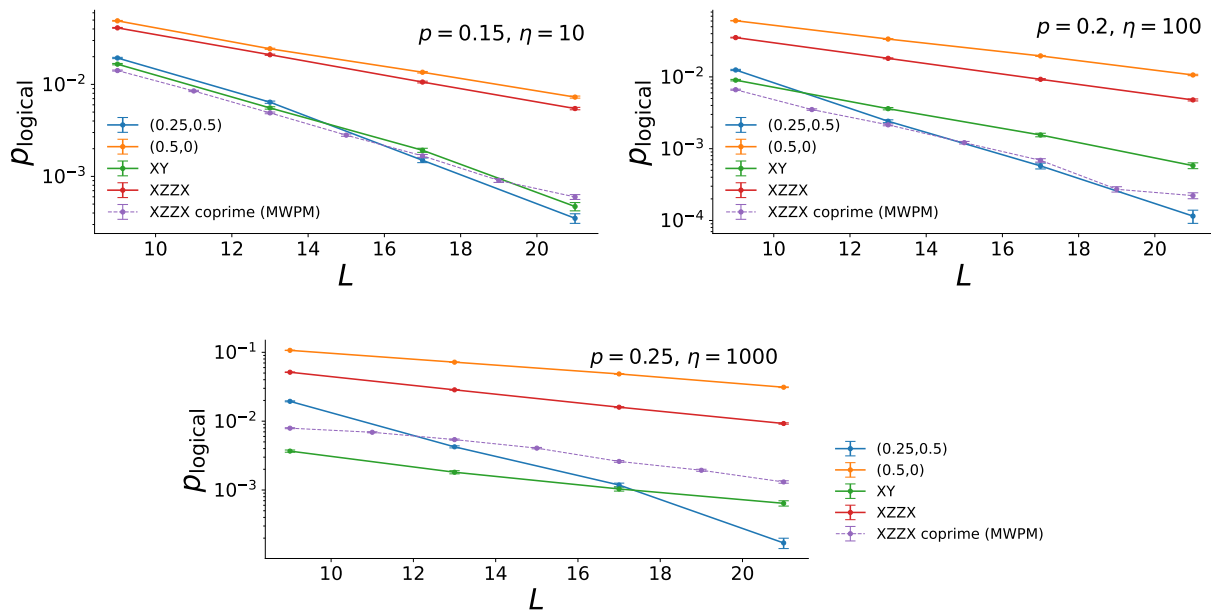


FIG. 7. Sub-threshold logical error rates of various CDSCs on the $L \times L$ square lattice for $p = 0.2$ and $\eta = 10, 100, 1000$. The performance of the XZZX code on a $L \times (L + 1)$ torus [7] using the MWPM decoder is included for comparison.

Appendix D: Performance of $(0.25, 0.5)$ and $(0.5, 0.0)$ random CDSCs

In Figs. 8 and 9 below, we plot the logical error rates of the random CDSCs $(0.25, 0.5)$ and $(0.5, 0.0)$ at different biases $\eta = 10, 30, 100, 1000$. The logical error rate for a particular random CDSC is calculated using 120 000 such runs using the BSV decoder for a set of physical error rates near the threshold p_c for code distances $L \in \{9, 13, 17, 21\}$. For these simulations, we used a large value of the bond dimension, $\chi = 56$. We observe that the decoder converges close to the threshold for this bond dimension at lower biases such as 0.5 and 10. However, close to the threshold at biases of 100 and 1000, we do not observe complete convergence. Hence, we confirm our threshold values by checking the exponential decay of logical error rate at rates below the threshold.

We also show the finite size scaling plots where we used the critical exponent method [19], *i.e.*, the values of thresholds were obtained from the logical error rate data

by doing finite size scaling analysis, *i.e.*, fitting the failure rate curves to the logical error rate $p_{\text{logical}} = A + Bx + Cx^2$, where A, B, C, p_{th} and ν are fitting coefficients, $x = (p - p_{\text{th}})L^{1/\nu}$ and p is the error rate. Note that p_{th} and ν correspond to the threshold and critical exponent, respectively.

Appendix E: Random CDSCs at large bias $\eta = 10^8$

We tested our conjectured phase diagram of 50% thresholds for random CDSCs, shown in Fig. 3(a) via tensor network numerics on a subset of random CDSCs, marked using green circles in Fig. 10(a) below.

In Figs. 10(b) and 11, we show the logical error rates vs physical error rates, obtained using the adaptation of the BSV decoder, for some representative random CDSCs characterized by (Π_{XZ}, Π_{YZ}) at a bias of $\eta = 10^8$. The numerical results are consistent with the infinite bias phase diagram for random CDSCs.

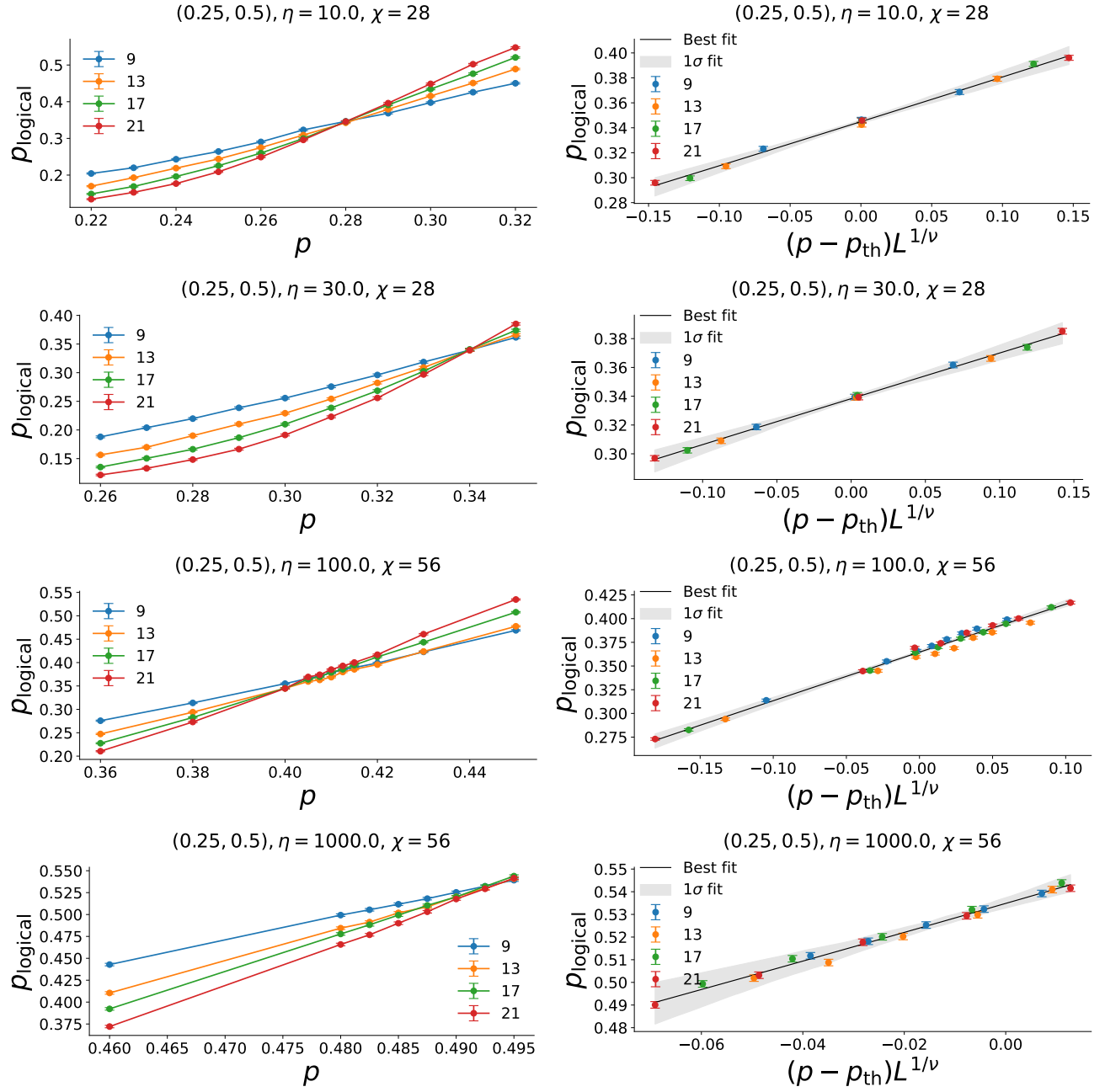


FIG. 8. Logical error rate p_{logical} versus physical error rate p and finite size scaling for the (0.25,0.5) random CDSC at different biases η and using bond dimension χ for the BSV decoder as indicated. Each data point for logical error rate p_{logical} is averaged over 120 000 Monte Carlo runs.

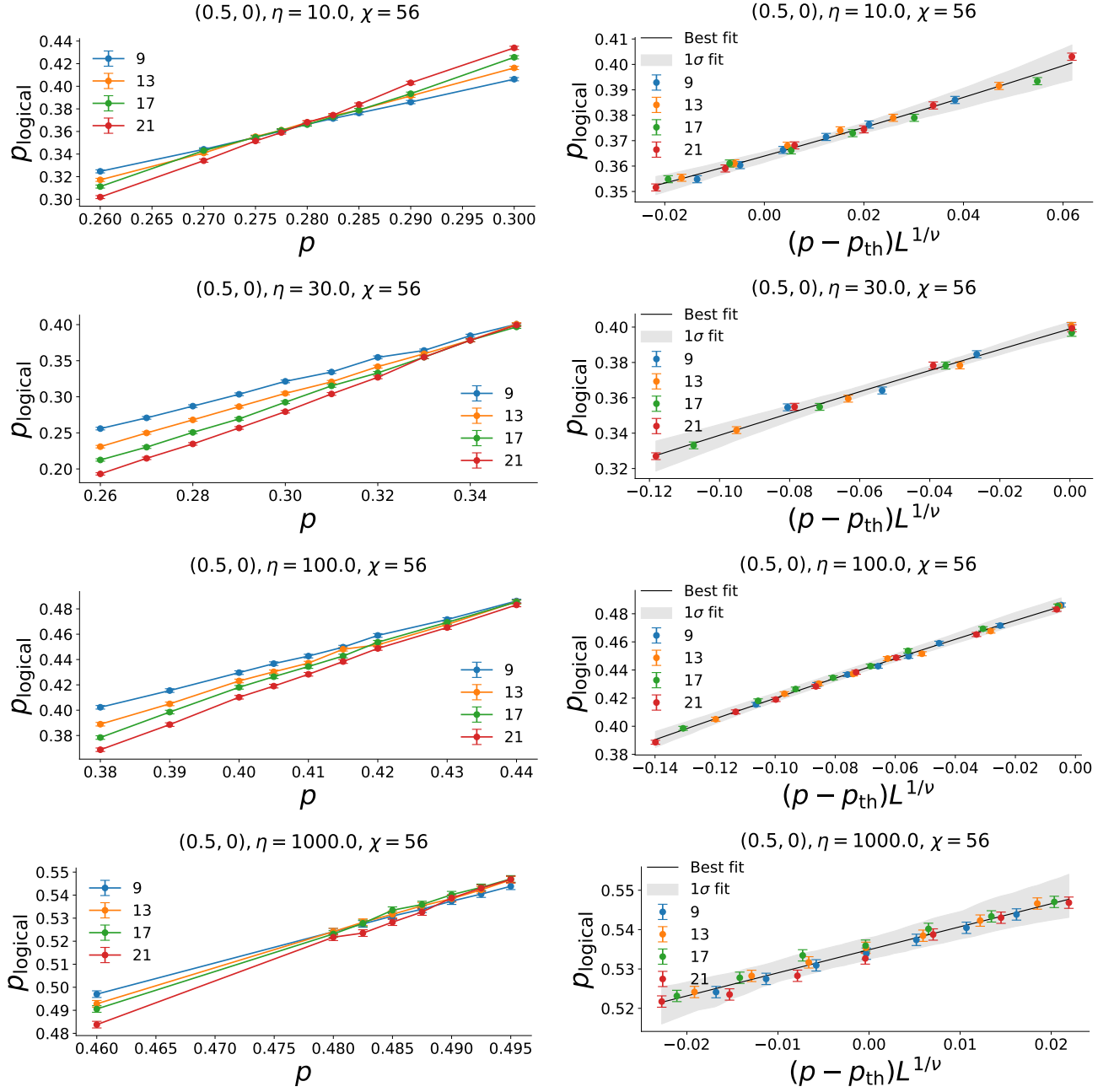


FIG. 9. Logical error rate p_{logical} versus physical error rate p and finite size scaling for the $(0.5, 0)$ random CDSC at different biases η and using bond dimension χ for the BSV decoder as indicated. Each data point for logical error rate p_{logical} is averaged over 120 000 Monte Carlo runs.

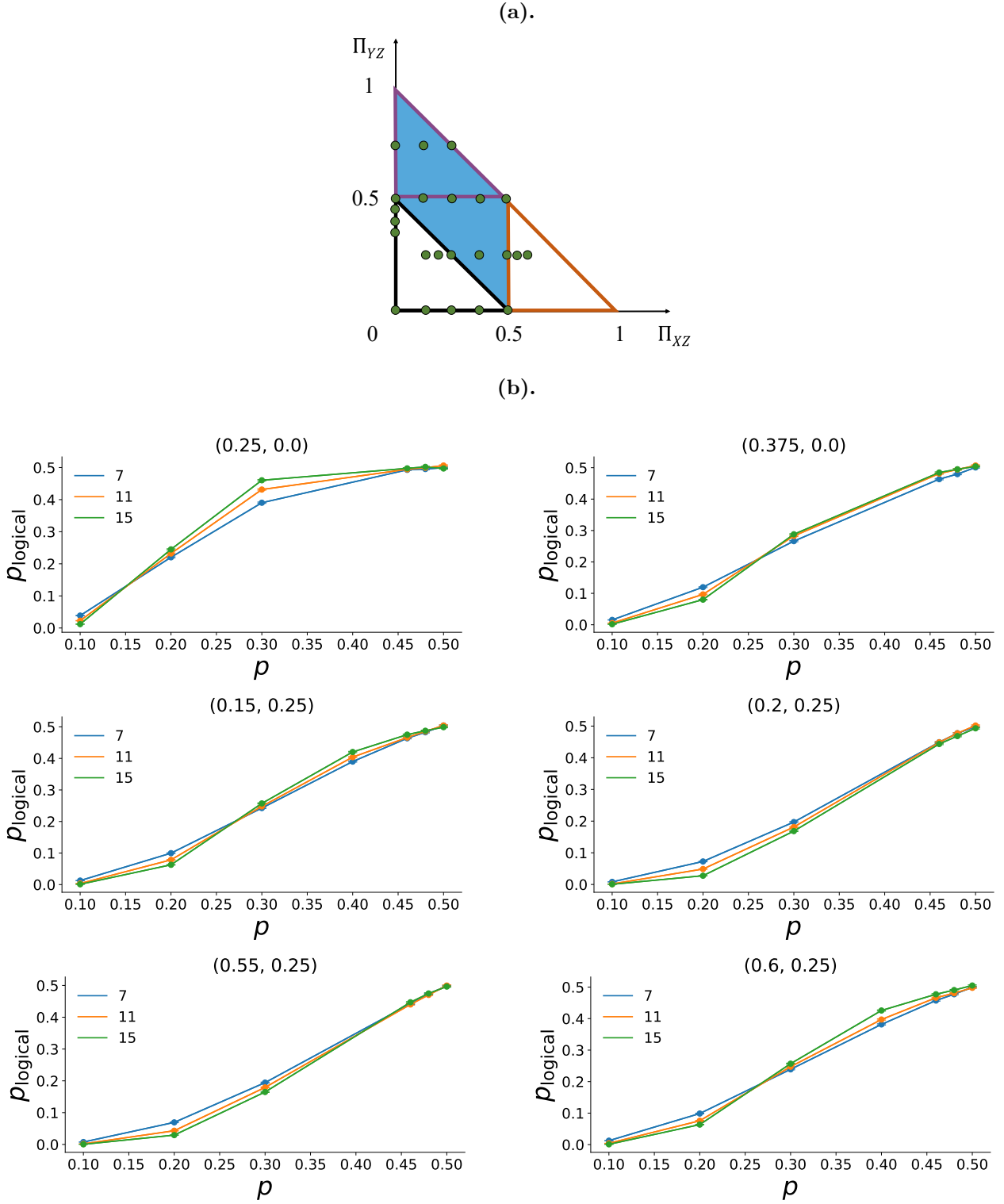


FIG. 10. (a) 50% threshold phase diagram from Fig. 3(a). The random CDSCs whose code performance was studied numerically are marked (green circles). (b) Performance of Random CDSCs outside the blue region (50% thresholds) of the phase diagram. Logical error rate p_{logical} versus physical error rate p for the (Π_{XZ}, Π_{YZ}) random CDSCs at bias $\eta = 10^8$. Each data point is averaged over 60 000 Monte Carlo runs of the BSV decoder with a bond dimension, $\chi = 56$.

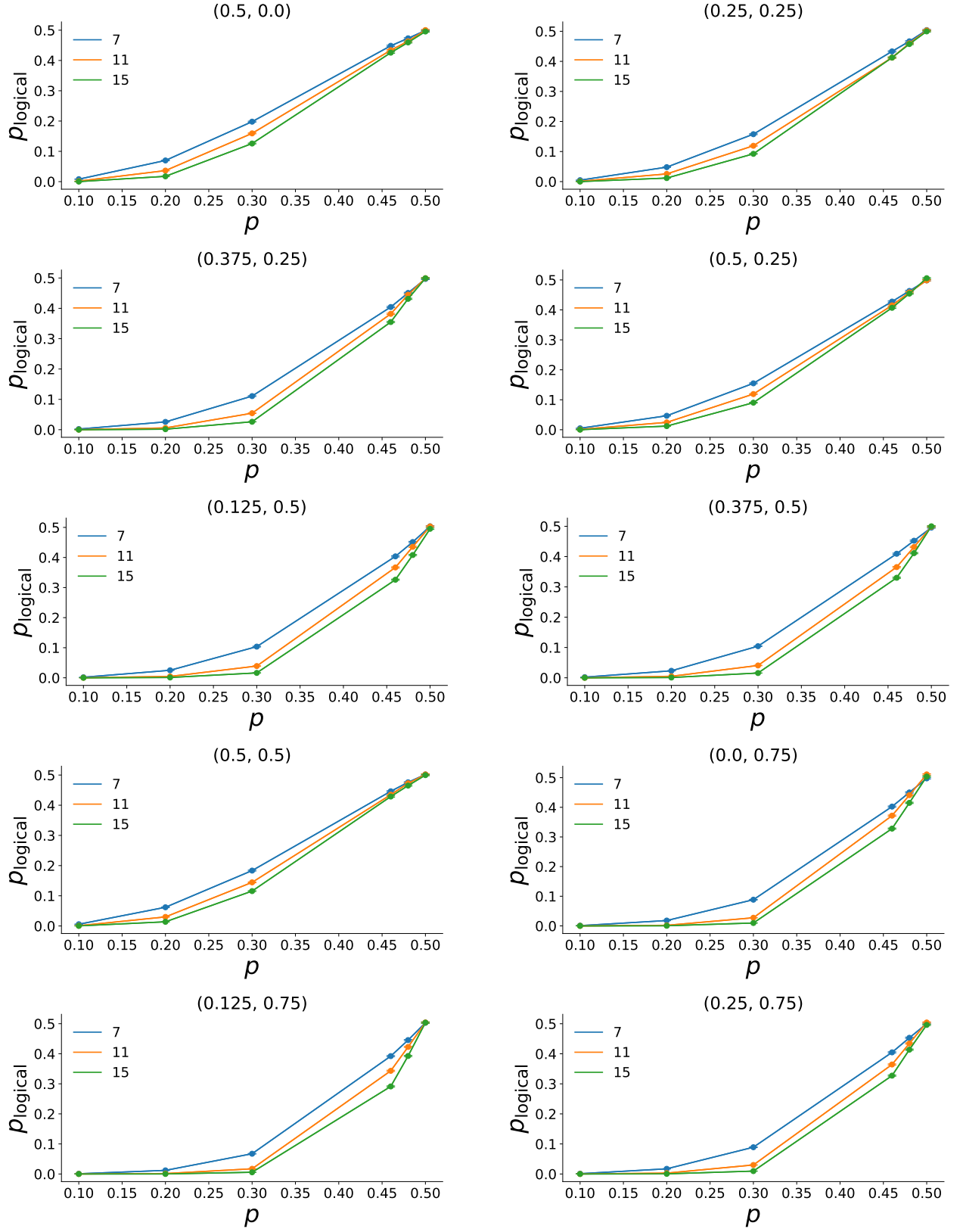


FIG. 11. Performance of Random CDSCs inside the blue region (50% thresholds) of the phase diagram. Logical error rate p_{logical} versus physical error rate p for the (Π_{XZ}, Π_{YZ}) random CDSCs at bias $\eta = 10^8$. Each data point is averaged over 60 000 Monte Carlo runs of the BSV decoder with a bond dimension, $\chi = 56$.